Master's thesis

NTNU
Norwegian University of Science and Technology
Faculty of Natural Sciences
Department of Physics

Ole Martin Granhus Kringlebotn

Climatology of gravity wave activity in Antarctica

Master's thesis in Physics
Supervisor: Patrick J. Espy
April 2020

NTNU
Norwegian University of
Science and Technology

Ole Martin Granhus Kringlebotn

Climatology of gravity wave activity in Antarctica

Master's thesis in Physics
Supervisor: Patrick J. Espy
April 2020

Norwegian University of Science and Technology
Faculty of Natural Sciences
Department of Physics

NTNU
Norwegian University of
Science and Technology

Abstract

Ground based measurements of the OH airglow layer have been done using a Michelson interferometer situated at Rothera (68°S, 68°W) over an eight year period spanning 2002-2009. This thesis explores whether or not OH can be used to monitor gravity wave activity in the MLT region of the atmosphere. Apart from interest on theoretical grounds, we are motivated by the need for improving our climate and long term weather models. From the intensity measurements of the OH Meinel (3, 1) band and the temperature estimates found from these measurements, a climatology is developed for both quantities. Our results are then compared to earlier work in order to investigate whether the variance in the temperature estimates can be used to measure gravity wave activity. We find that this is likely the case, especially for the first part of the year.

Sammendrag

Målinger har blitt gjort av natthimmellys fra OH ved å bruke et Michelson interferometer. Målingene ble gjennomført ved Rothera (68°S, 68°W) over en periode på åtte år fra 2002 til slutten av 2009. I denne oppgaven studeres det hvorvidt OH kan brukes til å observere tyngdebølgeaktivitet i mesosfæren og nedre del av termosfæren. Utover teoretisk interesse motiveres vi av et behov for å forbedre våre modeller for klima og langtidsvarsel. Fra målinger av intensiteten av OH Meinel (3, 1) båndet samt estimater for temperaturen, bygges det opp en klimatologi. Resultatene våre sammenlignes med tidligere arbeid for å se om variansen i temperaturestimatene kan brukes til å måle aktiviteten av tyngdebølgene. Vi finner dette til å være sannsynlig, spesielt for første delen av året.

Acknowledgements

This thesis is the product of research conducted during the final semesters of the two-year Master Program in Physics at the Norwegian University of Science and Technology (NTNU). I would like to thank my supervisor Prof. Patrick J. Espy for his guidance throughout this last year. For helping me to understand the physics, and for always answering my questions both via email and whenever I dropped by his office. Gratitudes are also extended to Magnus Ringerud for proofreading and valuable feedback. I want to thank Linjeforeningen Delta for making these last few years into the best years of my life. And last but not least I would like to thank my family for always supporting me.

Ole Martin Kringlebotn
Trondheim, Norway
April 2020

Table of Contents

Abbreviations

Explanation of abbreviations and acronyms that have been used throughout this thesis.

MLT	=	Mesosphere-Lower Thermosphere
MF Radar	=	Medium-Frequency Radar
MR	=	Meteor Radar
GW	=	Gravity Wave
PW	=	Planetary Wave
NWP	=	Numerical Weather Prediction
SEA	=	Solar Elevation Angle
HWM-93	=	Horizontal Wind Model
GCM	=	General Circulation Model
IR	=	Infrared
UV	=	Ultraviolet
IPCC	=	Intergovernmental Panel on Climate Change
WACCM	=	Whole Atmospheric Community Climate Model

Chapter 1

Introduction

Gravity waves are internal pressure oscillations in the atmosphere where buoyancy and gravity are the restoring forces on a displaced air parcel. The wave results in wave-like variations of the background density, temperature, and wind velocity of the atmosphere. There are many ways in which gravity waves can be generated in the lower atmosphere. For example, mountain waves. These waves can propagate up, preserving energy per volume, and then break and deposit its energy and momentum in the mesosphere and lower thermosphere (MLT). These waves are the primary way in which the atmosphere exchanges energy vertically, and the energy and momentum they deposit in the upper atmosphere drives a global circulation that can influence surface weather and climate. Since gravity waves can only be parameterized in climate and weather models, it is important to constrain these parameterizations, particularly in the Polar regions.

Since gravity waves perturb density and temperature, one method to remotely sense their flux in the upper atmosphere is to examine their effect on atmospheric emissions known as the airglow. At an altitude of about $87\,\mathrm{km}$ one finds a $\sim 8\,\mathrm{km}$ thick layer of OH^*. The hydroxyl radical is produced naturally in the atmosphere, mainly by the following reaction:

$$\mathrm{H} + \mathrm{O_3} \longrightarrow \mathrm{OH}^* + \mathrm{O_2}. \tag{1.1}$$

Here OH^* with vibrational levels $v =$ 6-9 are produced, and lower vibrational levels are subsequently produced through radiative cascading and collisional quenching. During these transitions infrared (IR) radiation is produced. This IR radiation can be measured from the ground. By using a Michelson interferometer the intensity of the OH Meinel (3, 1) band has been measured above Rothera ($68°$S, $68°$W) . From its brightness and the fact that it is approximately in thermal equilibrium with its surroundings, the temperature of the atmosphere at an altitude of $87\,\mathrm{km}$ can be calculated. This OH airglow layer can be perturbed by the aforementioned gravity waves and used to remotely sense the passage of gravity waves through this region. In this thesis we will explore whether the relatively

simple instrumentation used to measure OH airglow can be used to observe the gravity wave variance in the middle atmosphere in a climatological sense. Our observations will be compared with radar wind measurements of wind variance to assess their ability to characterize gravity wave effects. Additionally, features observed in the OH variance climatology will be interpreted in terms of seasonal changes in the underlying wind field.

1.1 Motivations for the thesis

In her PhD thesis de Wit (2015) discusses how when the Intergovernmental Panel on Climate Change (IPCC) presented their fourth Assessment Report in 2007 only four climate models extended above the stratospause. However, six years later when IPCC presented their fifth Assessment Report in 2013 all the ten highest model tops extended well into the mesosphere, with one going about $145\,\mathrm{km}$ up, well into the thermosphere. This development is due to the fact that extending our knowledge of the mechanisms higher up in the atmosphere is key to improving both our climate models, as well as our Numerical Weather Predictions (NWPs). The development of atmospheric model height in atmosphere-ocean general circulation models (GCMs) accompanied by a temperature profile of the atmosphere is shown in Figure 1.1.

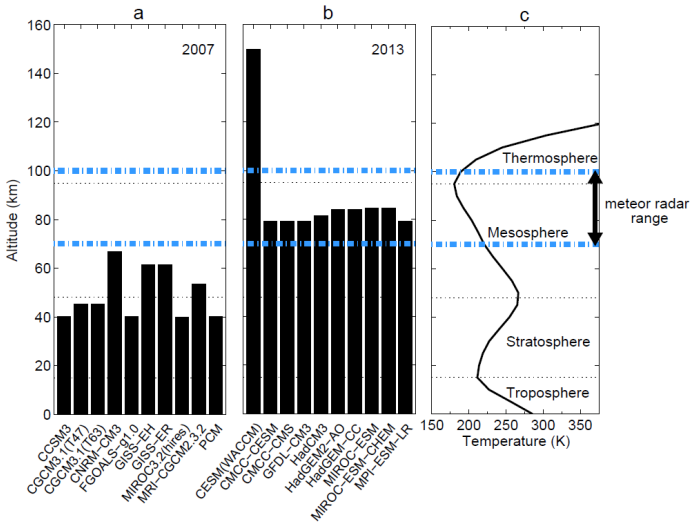

Figure 1.1: Development of atmospheric model top height in the atmosphere-ocean GCMs contributing to IPCC reports. Model top height of the ten GCMs with the highest model tops included in the IPCC report in (a) 2007 (IPCC, 2007) (from a total of 23 models), and (b) in 2013 (IPCC, 2013) (from a total of 52 models). (c) Temperature profile of the atmosphere, with the different regions indicated (based on CIRA-86 data (Fleming et al., 1990)). The horizontal black dotted lines indicate (from bottom to top): the tropopause, stratopause, and mesopause. The area between blue dash-dotted lines indicates the range of meteor radar wind observations. (de Wit, 2015)

The hydroxyl airglow layer is situated as mentioned in the MLT region. This is at the

boundary between the mesosphere and the thermosphere. Understanding the processes at the boundary between the layers of the atmosphere is key in obtaining a better understanding of the energy budget in the atmosphere. This is key, not just for improving our models, but for the general understanding of these two layers of the atmosphere, as well as the atmosphere as a whole.

1.2 Quantifying gravity wave activity through variance in temperature

Mitchell and Beldon (2009) have shown that by using a meteor radar (MR) in the MLT region, one can measure the wind speed and use the variance in wind speed as a proxy for gravity wave activity. Similarly Hibbins et al. (2007) have used a Medium-Frequency Radar (henceforth referred to as a MF radar) to do the same. From the theory of gravity waves, the following relationships are known:

$$\frac{\Delta T}{\overline{T}} \approx \frac{\Delta \rho}{\overline{\rho}} \approx \frac{\Delta v}{\overline{v}}, \tag{1.2}$$

where T is the temperature, ρ is the density, and v is the velocity of the gravity wave. Both Beldon and Mitchell (2009) and Hibbins et al. (2007) used the relationship between perturbations in wind velocity and perturbations in density to study gravity wave activity. In this thesis the relationship between the temperature perturbations and the perturbations in density will be examined. That is, whether or not measuring the variance in temperature using an interferometer can be used as a proxy for gravity wave activity will be explored. Ultimately one could develop a climatology from the variance in the temperature estimates.

1.3 Progress of this thesis

This thesis will progress in the following fashion: A description of the structure of the atmosphere with its different layers will be given. Further a quantum mechanical description of the OH molecule will be presented. The procedure for obtaining estimates for the temperature from measurements of intensity will be given. Then a brief description of how gravity waves are generated, and how they eventually deposit their energy and momentum is given. All of this will be presented in Chapter 2. The nature of the data is then presented. The necessary calculations for obtaining the variance and the relative variance for radiance and temperature will then be given, including the Krassovsky ratio of the radiance to temperature perturbation. In addition the correlation between the monthly average of the climatological daily variance in temperature and the amount of gravity waves blocked due to the background wind profiles will be studied. This analysis and the obtained results will be presented in Chapter 3. In Chapter 4 the trends in the results will be discussed, and compared to results obtained in other studies. Finally in Chapter 5 the conclusions that can be drawn from the results will be presented.

Chapter 2

Theory

2.1 Structure of the atmosphere

The atmosphere can be treated as having several layers with similar properties. Lund (2010) gives the following description of the structure of the atmosphere. From the ground up to about $15\,\mathrm{km}$ is the troposphere followed by the tropospause. The troposphere is characterized by a negative temperature gradient caused by a heating of the lower part due to radiative heating from the ground. Then from $20\,\mathrm{km}$ to $50\,\mathrm{km}$ one finds the stratosphere, bounded by the stratospause. The temperature gradient changes from negative to positive when going up to the stratosphere. This is due to heating of ozone by sunlight. Above that comes the mesosphere from about $50\,\mathrm{km}$ to $90\,\mathrm{km}$ bounded by the mesospause. The mesosphere is again characterized by a negative temperature gradient due to reduced solar heating, as well as increased radiative loss to space. Following the mesospause one finds the thermosphere. In the thermosphere high energy radiation from the sun is absorbed causing photoionization which again makes the temperature gradient change from negative to positive. The thermosphere reaches up to about $700\,\mathrm{km}$, and after that one reaches the exosphere. Only the first four layers will be discussed further throughout this thesis. The general structure is shown in Figure 2.1.

At about $87\,\mathrm{km}$ altitude with a width of about $8\,\mathrm{km}$ one finds the hydroxyl airglow layer (Lowe et al., 1996). Here OH^* is excited naturally through the following reaction (Lowe et al., 1996; Franzen et al., 2020; Pautet et al., 2014)

$$\mathrm{H} + \mathrm{O_3} \longrightarrow \mathrm{OH}^* + \mathrm{O_2}. \tag{2.1}$$

Since reaction (2.1) is highly exothermic (3.3 eV), it populates vibrational levels 6-9 of the product OH, here denoted as OH^*. This gives the following expression for the production rate of OH^*:

$$P(\mathrm{OH}^*) = k_{\mathrm{H+O_3}}[\mathrm{H}][\mathrm{O_3}]. \tag{2.2}$$

At night, this reaction is responsible for the majority of loss in ozone. The production mechanism for ozone is given by

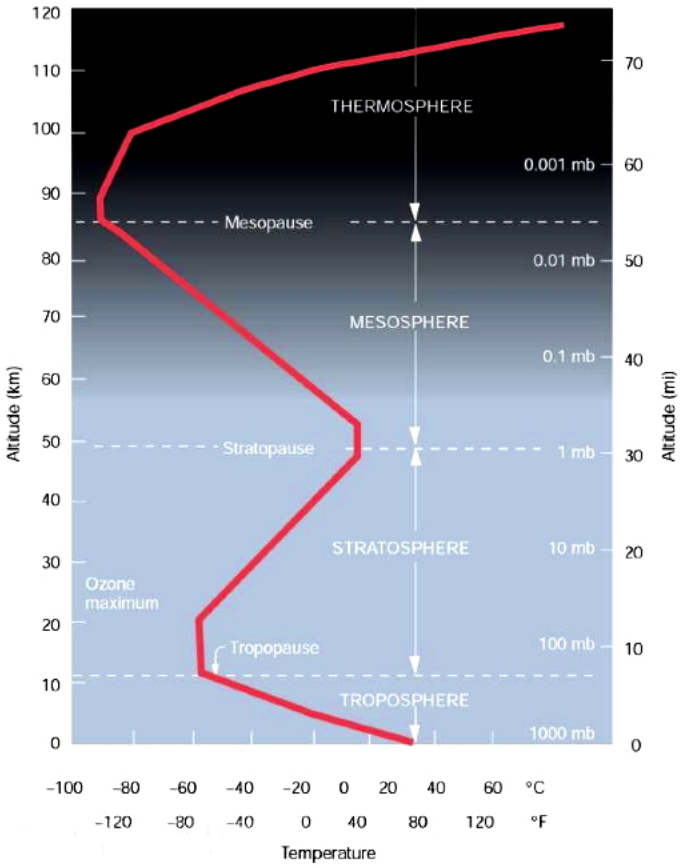

Figure 2.1: Vertical structure of the atmospheric temperature. The figure is from SFSU (2018, accessed 24.02.2020).

$$\mathrm{O} + \mathrm{O_2} + \mathrm{M} \longrightarrow \mathrm{O_3} + \mathrm{M}, \tag{2.3}$$

where M is a reaction mediator, typically $\mathrm{N_2}$ or $\mathrm{O_2}$ which are the most abundant species. Equating the loss and the production of ozone gives us the steady state concentration of ozone by the following equation:

$$[\mathrm{O_3}] = \frac{k_{\mathrm{O+O_2+M}}[\mathrm{O}][\mathrm{O_2}][\mathrm{M}]}{k_{\mathrm{H+O_3}}[\mathrm{H}]}, \tag{2.4}$$

which can be substituted into equation (2.2) to give the following production rate for excited hydroxyl at night:

$$P(\mathrm{OH^*}) = k_{\mathrm{O+O_2+M}}[\mathrm{O}][\mathrm{O_2}][\mathrm{M}]. \tag{2.5}$$

The thing to note now is that the concentration of ozone, as well as the concentration of excited hydroxyl, is proportional to the concentration of atomic oxygen. Atomic oxygen is created by photolysis through the known reaction

$$\mathrm{O_3} + \gamma \longrightarrow \mathrm{O_2} + \mathrm{O}, \tag{2.6}$$

where γ is an UVC or UVB photon from the sun. Seeing as this reaction takes place in the presence of sunlight, atomic oxygen will have to be produced in sunlit regions and then transported via horizontal or vertical motion for it to change the concentration in non-sunlit regions.

2.2 The OH-molecule and quantum mechanics

In this chapter a brief explanation of the origin of the Meinel (3, 1) band will be given. Most of the theory in this chapter was found in Lund (2010); Herzberg (1951); Hemmer (2005); McQuarrie and Simon (1997).

For a diatomic molecule like OH the energy can be written as a sum of the electronic energy, the rotational energy, and the vibrational energy in the following way by using the Born-Oppenheimer approximation (translational energy is excluded here):

$$E = E_e + E_r + E_v. \tag{2.7}$$

The electronic energy here is the energy associated with the electron orbits of the molecule. For a hydrogen atom this is fairly simple, however for diatomic molecules like the OH it becomes more complicated. For the hydrogen atom the electronic energy is given by

$$E_n = -\frac{\mu}{2\hbar^2}\left(\frac{Ze^2}{4\pi\epsilon_0}\right)\frac{1}{n^2}, n \in \mathbb{N}, \tag{2.8}$$

where μ is the reduced mass of the system given by $\mu = \frac{m_1 m_2}{m_1+m_2}$ and n is the main quantum number. Complete separation between the electron and the proton is defined as the zero energy. The so called ground state, which is the lowest energy state of the hydrogen, is the state with $n = 1$. For this text the thing to note is that for the electron to move between discrete energy values it can either emit a photon when going to a lower energy state, or absorb a photon in order to jump to a higher energy state. This photon will then have the energy and frequency, ν, given by:

$$h\nu = E_n - E_k = \Delta E = \left(\frac{e^2}{4\pi\epsilon_0}\right)\frac{\mu}{2\hbar^2}\left(\frac{1}{k^2} - \frac{1}{n^2}\right). \tag{2.9}$$

Classically the energy would be a continuous spectrum. In quantum mechanics however, this is not the case. The same principles as with the hydrogen atom also applies when looking at the OH-molecule. This thesis look at vibrational-rotational transitions within the ground electronic state of the OH-molecule. The first excited electronic state of the

OH-molecule lies 4.03 eV above the ground state and gives rise to transitions near $308\,\mathrm{nm}$. Since this upper electronic state is not populated in reaction (2.1), we need only look at transitions within the ground electronic state. These will consist of transitions between vibrational-rotational levels.

For the rotational energy a simple dumbbell model can be used. Here two masses are connected with a massless rod of length, r. In quantum mechanics this is given by

$$E_r = \frac{h^2}{8\pi^2 \mu r^2} J(J+1), J = 0, 1, 2... \tag{2.10}$$

where J is the rotational quantum number. Analogous to the electron spectra, the molecule can go from one rotational level to another by absorption or emission of a photon

$$\Delta E = h\nu = \frac{hc}{\lambda} \implies \frac{1}{\lambda} = \frac{\Delta E}{hc}, \tag{2.11}$$

where λ is the wavelength of the photon. By defining a rotational constant $B = \frac{h}{8\pi c \mu r^2}$, the rotational energy levels are given by the term values defined as

$$F(J) = \frac{E_r}{hc} = BJ(J+1). \tag{2.12}$$

A thing to note is that if the molecule is not a rigid rotor then there will be a correctional term due to the centrifugal force. This correction term however is about a factor 10^4 smaller than B for OH and can easily be ignored.

For the vibrational energy the molecule can be considered a harmonic oscillator as a first approximation, with displacement given by $r - r_e$ where r is the distance between the atoms, and r_e is the equilibrium distance. In quantum mechanics the energy of this harmonic oscillator is given by

$$E_v = h\nu(v + 1/2), v = 0, 1, 2... \tag{2.13}$$

where v is the vibrational quantum number and ν is the frequency of the oscillations. The energy can then be defined via the term values

$$G(v) = \frac{E_v}{hc} = \omega(v + 1, 2), \tag{2.14}$$

where ω is the harmonic wavenumber. The OH-molecule is not a harmonic, but an anharmonic oscillator, and the term values are given by

$$G(v) = \omega v - \omega x v^2 + \omega y v^3 + ... \tag{2.15}$$

where the ωx and ωy terms are small compared to ω, and as such the difference between energy levels decrease with increasing v. Another thing to note here is that the rotational constant B is dependent on r and is not strictly a constant. It should therefore be replaced by B_v with the subscript referring to the vibrational levels of the molecule. Note that by observing the spectrum one can see that the molecule makes over 100 vibrations over the course of 1 rotation. As a result, the molecule sees an inter-nuclear distance that is the average over these fast vibrations as it rotates. Thus, each vibrational level, which has its own average inter-nuclear distance, has a set of closely spaced rotational energy levels, given by equation (2.12), associated with it. A schematic of the relationship between the different energy levels is shown in Figure 2.2

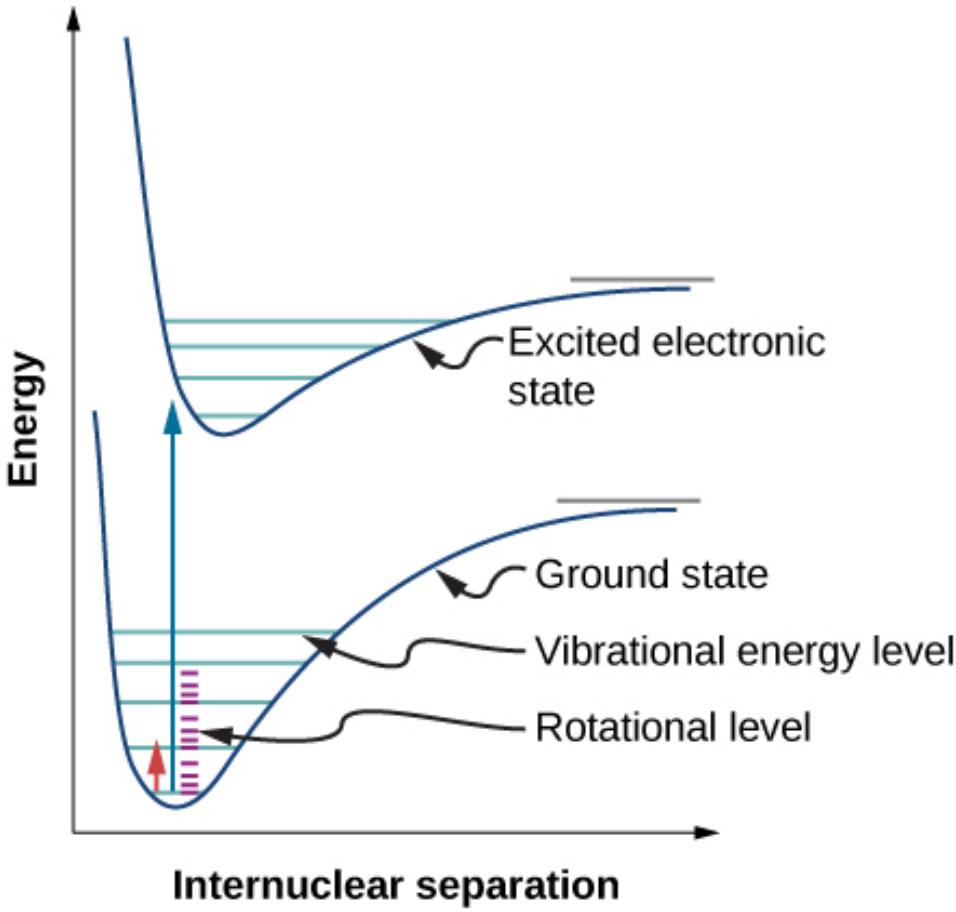

Figure 2.2: Three types of energy levels in a diatomic molecule: electronic, vibrational, and rotational. The blue arrow indicates going from the ground state to an excited electronic state, while the red arrow indicates a ro-vibrational transition (OpenStax, 2018, accessed 25.03.2020a).

Now one can consider the case where the molecule changes its vibrational and rotational levels at the same time. The set of all rotational transitions that can take place within

a given vibrational transition yields what is known as the rotational-vibrational bands. An example of such a band is the OH Meinel (3, 1) band studied here.

To get the wavenumber for these bands, the term values for the rotational and vibrational part need to be added. For the vibrational part one has

$$\tilde{\nu}_v = G(v') - G(v''), \tag{2.16}$$

while for the rotational part one has

$$\tilde{\nu}_r = F_{v'}(J') - F_{v''}(J''). \tag{2.17}$$

This can now be substituted into equation (2.12), where the subscript on the rotational constant B_v will be omitted. One then gets the following expression for the wavenumber:

$$\tilde{\nu} = \tilde{\nu}_v + B'J'(J'+1) - B''J''(J''+1). \tag{2.18}$$

Through selection rules from quantum mechanics the following constraints on ΔJ exist:

$$\Delta J = 0, \Delta J = \pm 1, \tag{2.19}$$

where the branch of lines with $\Delta J = 0$ is known as the Q-branch, the branch with $\Delta J = 1$ is called the R-branch, and the branch with $\Delta J = -1$ is called the P-branch. Substituting this into equation (2.18), and substituting from variables with double apostrophes to variables without apostrophes (e.g. $B'' \rightarrow B$), yields the following expressions for the wavenumber of the different branches:

$$\tilde{\nu}_Q = \tilde{\nu}_v + (B' - B)J + (B' - B)J^2, \tag{2.20}$$

$$\tilde{\nu}_R = \tilde{\nu}_v + 2B' + (3B' - B)J + (B' - B)J^2, \tag{2.21}$$

and

$$\tilde{\nu}_P = \tilde{\nu}_v - (B' + B)J + (B' - B)J^2. \tag{2.22}$$

A schematic depiction of the rotational energy levels imposed on the vibrational transition from $v = 0$ to $v = 1$ is shown in Figure 2.3.

From reaction (2.1) the excess heat of the reaction yields OH^* with vibrational quantum levels v = 6-9, see Lund (2010); Franzen et al. (2020) and references therein. Subsequent radiative cascading and collisional quenching produces OH^* with all vibrational levels $v \leq 9$. Radiative deactivation can occur between any two vibrational levels, but transitions with $\Delta v = 2$ are preferred (Franzen et al., 2020). Collisional quenching is the process where the molecule collides with another atom or molecule, and thereby transfers some of its vibrational energy into kinetic energy in the other atom or molecule. The concentration of OH^* with a given vibrational level $v < 6$ is proportional to the concentration of OH^* with $v > 6$, which again is proportional to the concentration of atomic oxygen. This means that OH^* with $v = 3$ is proportional to the concentration of atomic oxygen.

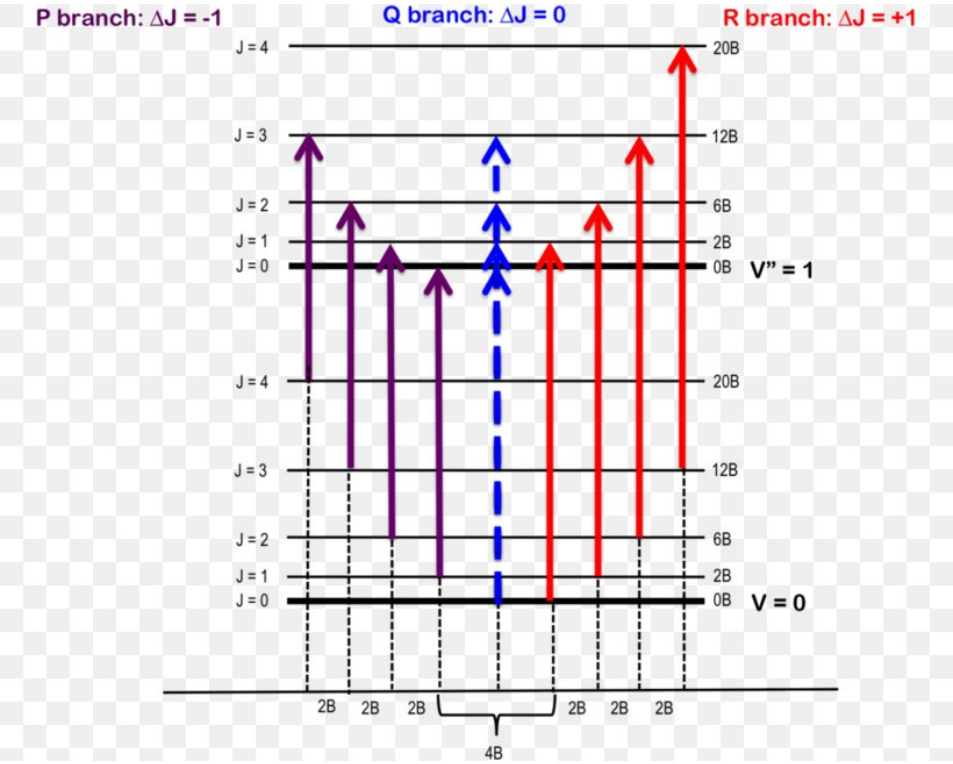

Figure 2.3: Depiction of rotational energy levels, J, imposed on vibrational energy levels, v. The transitions between levels that would result in the P- and R-branches are depicted in purple and red, respectively, in addition to the theoretical Q-branch line in blue (OpenStax, 2018, accessed 25.03.2020b).

2.3 Estimating the temperature

As mentioned earlier a Michelson interferometer was used to measure the intensity (intensity and radiance will be used interchangeably throughout this thesis) of the OH Meinel (3, 1) band. The temperature of the surrounding mesosphere can be estimated from these measurements. From measurements of intensity one can derive the rotational temperature by assuming a Boltzmann distribution of the rotational level populations. For the OH Meinel (3, 1) band this is a reasonable assumption (Franzen et al., 2020). Most of the theory in this chapter was found in Franzen et al. (2017, 2020); Lund (2010) and references therein. As discussed in Chapter 2.2 reaction (2.1) yields OH^* with vibrational quantum levels $v = 6$-9. Lower vibrational levels are reached by subsequent radiative cascading and collisional quenching. These processes take some time and, on average, a molecule undergo at least 10 collisions before emitting a photon. By that time it will be in thermal equilibrium with its surroundings. The derived rotational temperature will then be approximately equal to the kinetic temperature of the mesosphere. The intensity of each rotational line can then be calculated as follows:

$$I(v', v, J', J) = A(v', v, J', J)C(v', J')(2J' + 1)e^{-\frac{E(v', J')}{kT}}, \tag{2.23}$$

where $A(v', v, J', J)$ are the Einstein coefficients for spontaneous emission from one rovibrational transition, and $C(v', J')$ is the total population of the v' state. The values for the Einstein coefficients used in this thesis were taken from Mies (1974). While newer coefficients are available, the Mies coefficients were used in order to infer temperatures that could be be compared with earlier observations. The unknown quantities now are the temperature, T, and the total population of the v' state, $C(v', J')$. Seeing as many rotational lines are measured these can be approximated by a standard least squares fit.

Michelson interferometer observations of the OH Meinel (3, 1) band nightglow were made in the spectral region between 1000 and $1700\,\mathrm{nm}$ at $\sim 0.5\,\mathrm{nm}$ resolution in order to measure the OH intensity (Espy et al., 2007). Each scan give rise to an interferogram. Interferograms were scanned in ~ 3 seconds and summed to a single individual spectrum, with an integration time of ~ 5 minutes. By weighting the contribution of each individual rotational line by the unit area line function of the instrument (here a Hamming function), a synthetic spectrum was created for each spectral position, i. The intensity at point i is given by the following expression:

$$I_i = C(v', J') \sum_{J'} w_{i,J'} A(v', v, J', J)(2J' + 1)e^{-\frac{E(v', J')}{kT}}, \tag{2.24}$$

where $w_{i,J'}$ is the line shape function. With the initial estimates for the temperature and the total population of the v' state, one can now create a model synthetic spectra at each data point. The difference between the measured spectra, M_i, and the model synthetic spectra, I_i, can be equated to the changes in temperature and total population via the Jacobians:

$$M_i - I_i = \frac{\partial I_i}{\partial T} dT + \frac{\partial I_i}{\partial C(v', J')} dC(v', J'), \tag{2.25}$$

which gives a set of individual equations for each datapoint, i, and dT and $dC(v', J')$ are found by least square fitting. These then give corrections to the a priori estimates, and the process is repeated until the best fit is observed.

2.4 Gravity waves

A gravity wave, sometimes known as a buoyancy wave, is a wave caused by dense matter being raised to a higher altitude than less dense matter. In the atmosphere this translates into raising a parcel of air up to a higher altitude while cooling it adiabatically. Here the surrounding air is less dense, and gravity will then act on the parcel of air and drag it back down. Due to adiabatic heating the parcel will now be less dense than the surrounding air, and buoyancy will push it back up. In other words the parcel of air will oscillate with gravity and buoyancy as its restoring forces. Gravity waves can originate from a number of scenarios. The main processes are air flow over topography (resulting in orographic gravity

waves) and convection (non-orographic gravity waves) (de Wit, 2015). To get a clear picture of the physics Hocking (2001, accessed 24.02.2020a) look at a corrugated sheet being moved through a fluid. A corrugated sheet moving at constant speed, c, through a fluid is shown in Figure 2.4.

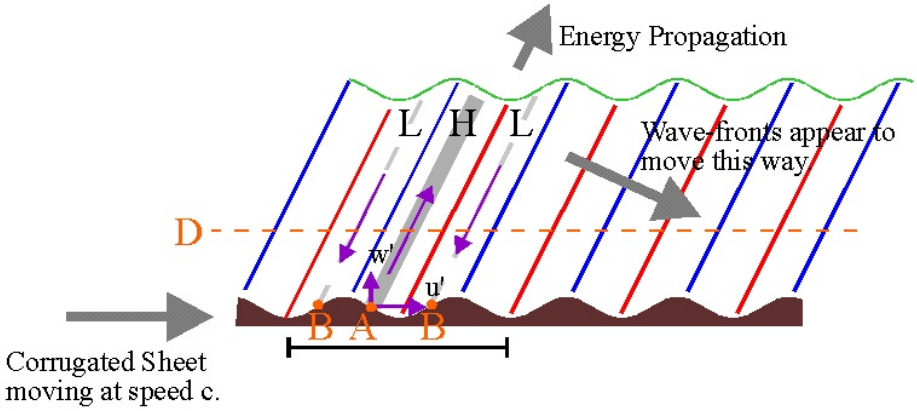

Figure 2.4: Corrugated sheet moving through a fluid. The figure is from Hocking (2001, accessed 24.02.2020b).

A particle at point A will after a short time, Δt , be pushed upwards and forwards. Particles at point A will therefore receive a velocity component, w', in the vertical direction, and a velocity component, u', in the horizontal direction. Conversely at point B the ground will appear to have fallen away and thus the velocity components here will point downward and to the left. At point A due to the compression of the air you will get a region of high pressure, and conversely a region of low pressure at point B. Air along the blue lines will be the ones that are most displaced upwards, and will be subject to the largest amount of adiabatic cooling. Parcels of air on the red lines however will be to ones that are displaced downwards the most, and will therefore be subject to the largest amount of adiabatic heating. These regions will follow the corrugations, and therefore to an outside observer the wavefronts will appear to propagate downwards to the right. The rate of which these wavefronts appear to propagate is called its phase speed. Note that the wavefronts on Figure 2.4 is not to scale. A typical gravity wave can have vertical wavelengths of about $10\,\mathrm{km}$ to $20\,\mathrm{km}$, while the horizontal wavelength can reach several hundreds or even thousands of kilometers. Seeing as the parcels of air at point A were given velocity components upwards and to the right, this will be the direction of propagation for energy and momentum (the direction of the group velocity).

For the upward propagation of gravity waves in the atmosphere, the phase speed is of great importance. As the horizontal phase speed approaches the background mean wind speed, the wave breaks and dissipates its energy and momentum. This will have a small impact on the background wind at low altitudes where the density is still high. However at higher altitudes where the density of the background air is low, the dissipation

of gravity wave momentum will significantly affect the mean winds. This also means that the background winds will filter out some of the gravity waves before they reach the hydroxyl layer. This gravity wave filtering is shown in Figure 2.5.

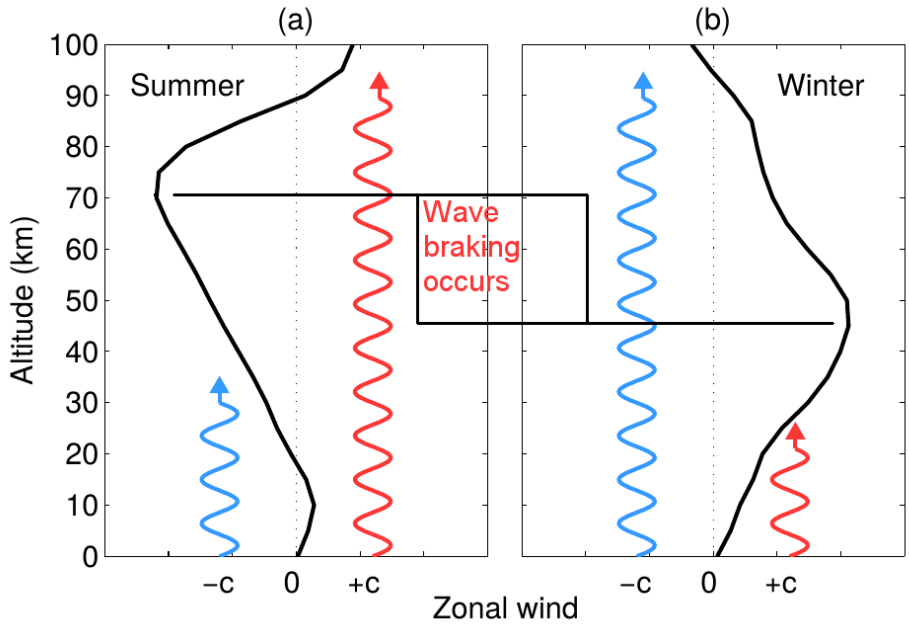

Figure 2.5: Illustration of GW filtering. Zonal wind profiles (black line) at 60°N for (a) summer and (b) winter. Blue lines are westward ($c < 0$) GWs and red lines are eastward ($c > 0$) GWs. The figure is from de Wit (2015).

Here the black line is indicating a typical wind profile for 60°N, and here c is the horizontal phase speed of the gravity waves. In the left part of the figure one sees the northern hemisphere summer, where mainly gravity waves with eastward momentum can reach the MLT region, while waves with westward momentum is blocked in the underlying atmosphere. Conversely in the right part of the figure summer is shown. Here mainly gravity waves with westward momentum reaches the MLT, while waves with eastward momentum break at a lower altitude.

Gravity waves are the primary way in which the atmosphere exchanges energy vertically, and the energy and momentum they deposit in the upper atmosphere drives a global circulation. The mean mesospheric temperature at the winter pole is higher than the summer pole. At the pole in the summer hemisphere the days are longer, and as such more sunlight heat the stratosphere. Conversely the winter pole will receive less sunlight, and the stratospheric temperature will be lowered. As the temperature changes this will create a summer pole with a higher pressure, and a winter pole with lower pressure in the

stratosphere. This difference in pressure causes a thermal wind from the summer pole towards the winter pole. The coriolis force then acts on the thermal winds and creates westward winds on the summer hemisphere, and conversely eastward winds on the winter hemisphere. The westward winds on the summer hemisphere will then block all gravity waves with horizontal phase speed equal the background wind speed. As a consequence only gravity waves with phase speeds directed eastwards will be able to rise up to the mesosphere. The eastward winds on the winter hemisphere will block gravity waves with eastward phase speeds in the same manner. The gravity waves that do end up in the mesosphere will act as a drag force, causing a mesospheric wind from pole to pole. In the summer hemisphere the wind will move towards the equator, while in the winter hemisphere the wind will be poleward. This meridional circulation causes an upward motion at the summer pole, bringing air poor in oxygen up to the OH airglow layer. Conversely it causes a downward motion at the winter pole, bringing air rich in oxygen to the OH layer. A consequence of the upward motion at the summer pole is that, as a parcel of oxygen poor air rises upwards its pressure will drop, which will cause adiabatic cooling. Conversely the downward motion at the winter pole causes the oxygen rich air to be heated adiabatically. This adiabatic heating and cooling explains the change in mean mesospheric temperatures between the winter and summer mentioned above.

As shown gravity waves have a huge impact on the climate, and therefore it is important to quantify the energy and momentum flux due to gravity wave activity when developing climate models, like the Whole Atmospheric Community Climate Model (WACCM), and NWPs. Gravity waves are however of too small a scale to be directly represented in the models by a simple physical process, and as such it needs to be parameterized. WACCM is a high-top, highly-coupled model, where a change made to improve one aspect of the simulation can make something else worse. It is therefore of key importance to obtain good constrains to the models.

Chapter 3

Analysis and results

The purpose of this analysis is to investigate whether the variance in the radiance and temperature can be used as a proxy for gravity wave activity. This would be more or less analogous to the variance technique as presented by Beldon and Mitchell (2009) and Hibbins et al. (2007) for horizontal wind velocities. The format of the data used will be described. Further the methods used to find the variance, as well as relative variance and the Krassovsky ratio, will be presented. Finally data for the monthly background wind profiles from Hibbins et al. (2005) will be used to look at gravity wave blocking, and how it correlates to the changes in variance.

3.1 Data

The data used in this thesis is obtained from a scanning Michelson interferometer at the British Antarctic Survey station at Rothera, Antarctica (68°S, 68°W) (Espy et al., 2003). The data spans eight years from 2002 - 2009, and includes info about the hour of the day and what day of the year it was gathered, as well as the current solar elevation angle, SEA. The data includes values for the radiance of the OH Meinel (3, 1) band, in kR, and derived temperatures, in K. In addition it includes values for the uncertainties in both radiance and temperature, which are estimated by a standard least squares fitting procedure (Espy et al., 1987; Espy and Stegman, 2002). The unit Rayleigh (R) was first defined by Hunten et al. (1956) as follows:

$$1\mathrm{R} := 10^{10}\ \text{photons}\ \mathrm{s}^{-1}\mathrm{m}^{-2}\mathrm{col}^{-1}. \tag{3.1}$$

Baker and Romick (1976) has shown that the following definition is self-consistent for use with photon radiance

$$1\mathrm{R} := \frac{10^{10}\ \text{photons}}{4\pi}\mathrm{s}^{-1}\mathrm{m}^{-2}\mathrm{sr}^{-1}. \tag{3.2}$$

This gives the following approximate relationship to watts in the case of the OH Meinel (3, 1) band

$$1\mathrm{R} \approx 1.05 \cdot 10^{-12} \frac{\mathrm{W}}{\mathrm{m}^2 \cdot \mathrm{sr}}. \tag{3.3}$$

Each day of the year has several measurements, with time between measurements ranging from 15 minutes to a few hours. In the dataset some measurements are corrupted and some nights have none or very few measurements, either due to cloudy weather or technical difficulties. Too few measurements will give us a bad estimation for the variance, and as such only nights with ten or more measurements will be used. In addition the only measurements of interest are those when the sun is down. That is mainly because of photolysis of ozone due to sunlight, as well as difficulties distinguishing radiation due to OH^* from solar radiation. The following approximation for the relationship between altitude and solar elevation angle (angle from the horizon), SEA, in degrees, θ, exists:

$$\theta \approx \sqrt{z}, \tag{3.4}$$

where z is the altitude of the Earth's shadow in km. The atmosphere will be in darkness below this altitude when the Sun is below the horizon ($\theta < 0$). Here $100\,\mathrm{km}$ is used as a value for z, which means only measurements with $\theta < -10^\circ$ will be included in the analysis. The data used can be found at British Antarctic Survey UK Polar Data Centre (2016, accessed 04.04.2020).

3.2 Climatology of radiance and temperature

Now that the restrictions on the dataset is clear, the first thing to do is to provide some mathematical definitions that will be used throughout this section. For a measured quantity, x, with an estimated uncertainty, δx, and a given number of measurements, N, one defines the weighted arithmetic mean as follows:

$$\overline{x} = \frac{\sum_i^N \frac{x_i}{\delta x_i^2}}{\sum_i^N \frac{1}{\delta x_i^2}}, \tag{3.5}$$

where the subscript denotes measurement number i. As an estimator for the uncertainty of the weighted arithmetic mean one uses the standard error of the mean, Δx, which is defined as follows:

$$\Delta x = \sqrt{\frac{1}{\sum_i^N \frac{1}{\delta x_i}}}. \tag{3.6}$$

Finally one defines the variance, σ_x^2, of the measured quantity, x, as follows:

$$\sigma_x^2 = \frac{\sum_{i=1}^{N} (x_i - \overline{x})^2}{N-1}. \tag{3.7}$$

The calculations that follow in this section are done in the same manner for both the temperature and the radiance.

Now that the restrictions on the dataset are clear, and the general statistical quantities of interest have been defined, the first thing to do is to use equation (3.5) to find the daily mean for each night with ten or more measurements where the sun has an SEA $< -10^\circ$ (that is, darkness below $100\,\mathrm{km}$). The daily mean is calculated for each day of measurement (hereafter referred to as DoM). Further equation (3.6) is used to estimate the uncertainty of the daily mean for each DoM. The daily mean and its estimated uncertainty is then used to calculate the climatological daily mean, $\langle\overline{x}\rangle$, for each day of year (hereafter referred to as DoY) using equation (3.5) and summing over all corresponding DoYs with valid measurements. A thing to note here is that two of the years of measurement are leap years, so February 29th is day number 60. For the other years of measurements, all days after February are shifted by one.

Equation (3.7) yields the daily variance for each of the quantities for each DoM. Further the climatological daily variance, $\overline{\sigma_x^2}$, is found by averaging the daily variance for all corresponding DoYs with valid measurements. The climatological daily variance and mean for temperature is showin in Figure 3.1a and 3.1b respectively. Likevise the climatological daily variance and mean for radiance is shown in Figure 3.2a and Figure 3.2b respectively. For both the climatological daily variance and mean a three term Fourier fit was included. The choice of three terms comes from studies by Lund (2010); Espy and Stegman (2002) that have looked at the number of significant harmonics in comparable data. Lund (2010) show for this dataset that higher level harmonics approaches the error of the individual measurements. The main purpose of the fit for this thesis is to help guide the eye, rather than to study the harmonics themselves.

The relative variance of a quantity is given by the ratio between the square root of the variance (i.e. the standard deviation) and the mean for that quantity. It is a standard measure for the dispersion of a probability distribution. Note that it should only be used for data that are measured using a ratio scale with a well defined zero, which holds in this case. It is also a dimensionless quantity, and can be used to compare quantities of different units. In effect it means that a quantity that has a larger relative variance will vary more than a quantity with a lower relative variance. For this thesis the climatological relative variance was calculated as follows:

$$RV_x = \frac{\sqrt{\overline{\sigma_x^2}}}{\langle\overline{x}\rangle} \cdot 100\%. \tag{3.8}$$

This is not strictly the same as calculating the ratio between the daily standard deviation and the daily mean before averaging to find a value for an average year, but the difference

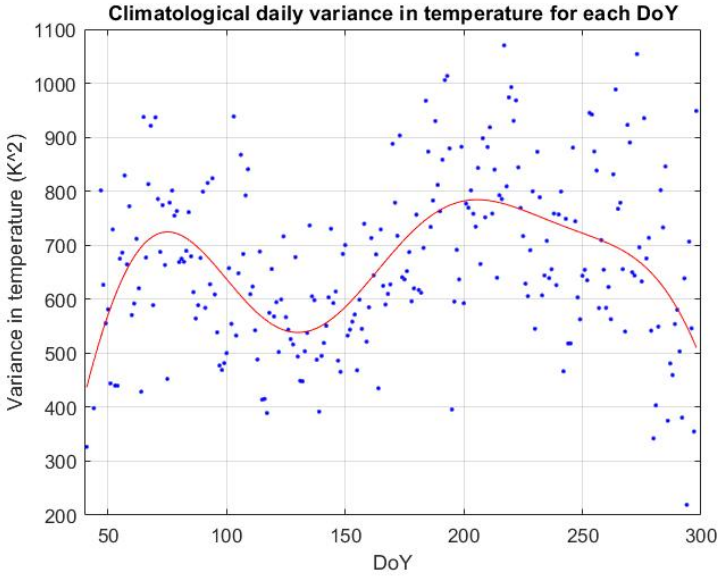

(a) Climatological daily variance in temperature for each DoY.

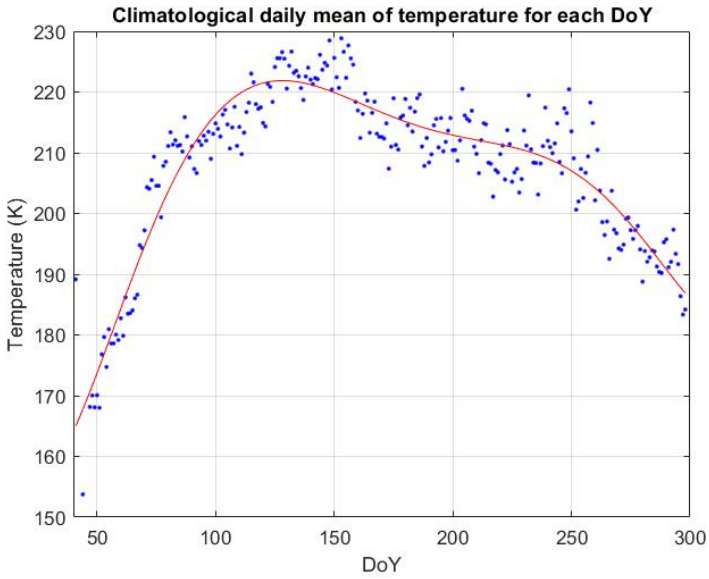

(b) Climatological daily mean of temperature for each DoY.

Figure 3.1: Scatter plot showing climatological daily variance and mean for each day of year for temperature. A three term Fourier fit is included to help guide the eye.

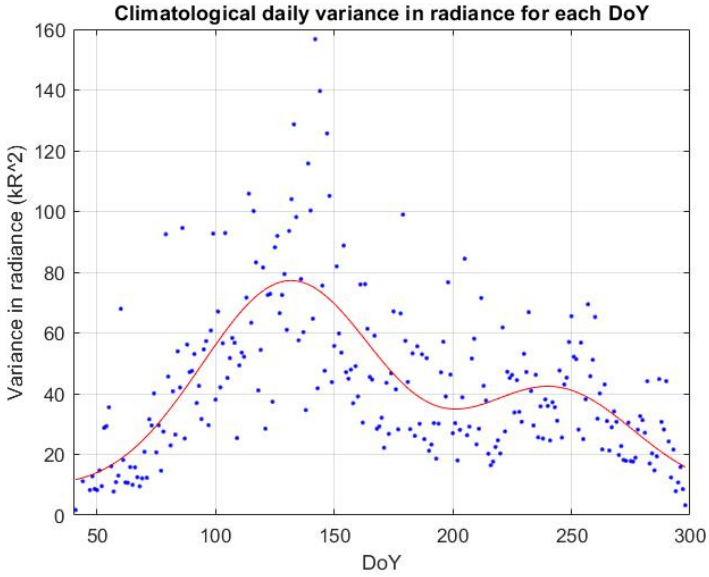

(a) Climatological daily variance in radiance for each DoY.

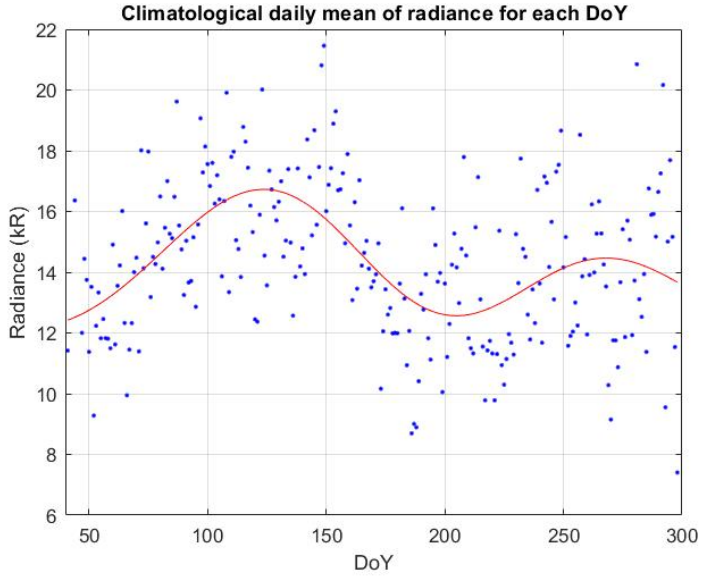

(b) Climatological daily mean of radiance for each DoY.

Figure 3.2: Scatter plot showing climatological daily variance and mean for each day of year for radiance. A three term Fourier fit is included to help guide the eye.

here is negligible. The climatological relative daily variance, with a red horizontal line showing the yearly average, for temperature and radiance is shown in Figure 3.3a and Figure 3.3b respectively.

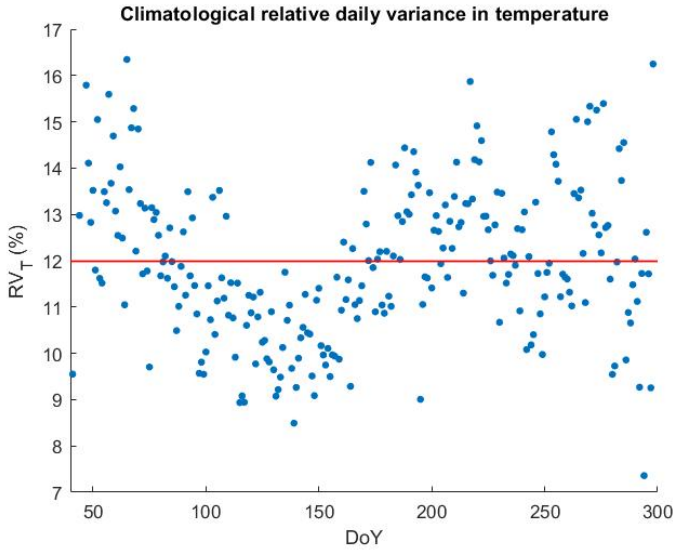

(a) Climatological relative daily variance in temperature.

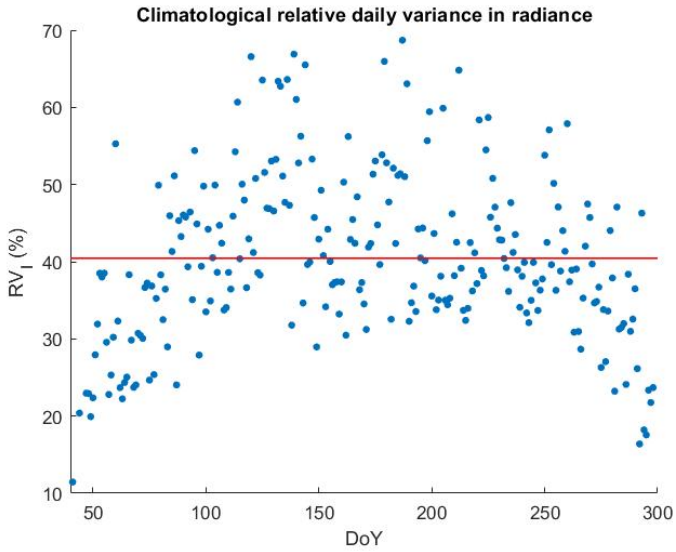

(b) Climatological relative daily variance in radiance.

Figure 3.3: Scatter plot showing the climatological relative daily variance for each DoY with a red line showing the yearly average.

3.3 The Krassovsky ratio

Once the climatological relative daily variance has been found, it is of interest to find the Krassovsky ratio, which is the ratio of the wave's relative airglow intensity fluctuation to its relative temperature fluctuation. The airglow will have an intensity that can vary with latitude and longitude. Part of this is due to species variation, and part is due to the latitudinal and longitudinal variation of temperature. The Krassovsky ratio has been studied by Hines and Tarasick (1987); Swenson and Gardner (1998); Liu and Swenson (2003); Hickey and Yu (2005) and is, in essence, a measure to see whether two waves with different measurements for amplitude and fluctuations are similar. That is, it is a tool to compare measurements done at different latitudes, longitudes, and at different temperatures. It also allows one to compare measurements of airglow emissions from different species (e.g, compare O_2 and OH).

From equation (2.5) and the fact that the production of excited hydroxyl at night is proportional to the radiance, one obtains the following relationship:

$$I \propto k_{\mathrm{O+O_2+M}}(T)[\mathrm{O}][\mathrm{O_2}][M] \propto k(T)\rho^2[\mathrm{M}], \tag{3.9}$$

where I is the radiance. The Krassovsky ratio was developed on the basis that the relative intensity fluctuation should cancel out the part of the enhancement factor due to the density enhancement of the wave. Since the temperature is derived by integrating through the airglow, the relative temperature fluctuation should remove the effect of the changing intensity and temperature profiles on the integrated temperature. Dividing the two should cancel out any cross terms, like the temperature changing the rate coefficients. The Krassovsky ratio, η, for the averaged values is calculated here using the following ratio:

$$\eta_{\mathrm{DoY}} = \frac{\frac{\sqrt{\overline{\sigma_I^2}}}{\langle \overline{I} \rangle}}{\frac{\sqrt{\overline{\sigma_T^2}}}{\langle \overline{T} \rangle}}. \tag{3.10}$$

To better see the day-to-day variability, the ratio was also calculated for each DoM using the following ratio:

$$\eta_{\mathrm{DoM}} = \frac{\frac{\sigma_I}{\overline{I}}}{\frac{\sigma_T}{\overline{T}}}. \tag{3.11}$$

Figure 3.4a show the Krassovsky ratio of the average values for each DoY with a fitted horizontal line for the average of said values. Averaging each η_{DoM} instead would give close to the same values, and are included as a dashed horizontal line for completeness sake. The Krassovsky ratio for each DoM is shown in Figure 3.4b.

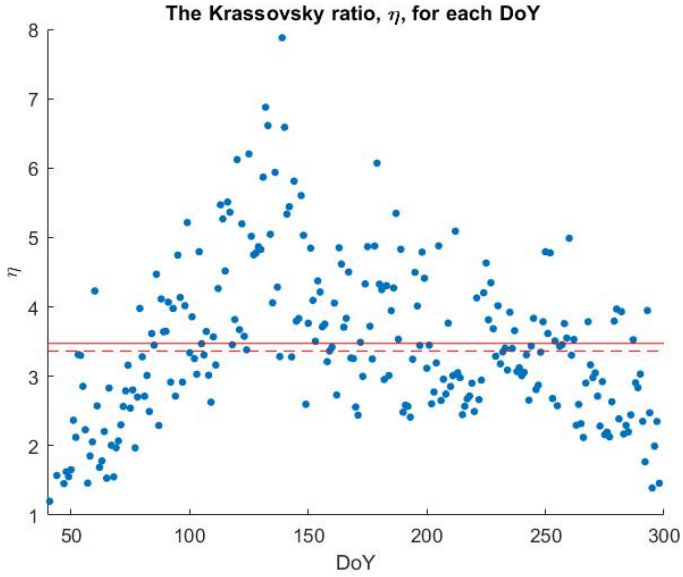

(a) The Krassovsky ratio of averaged values for each DoY, with red horizontal line showing the average value, and a red dashed horizontal line showing the average of all values from Figure 3.4b.

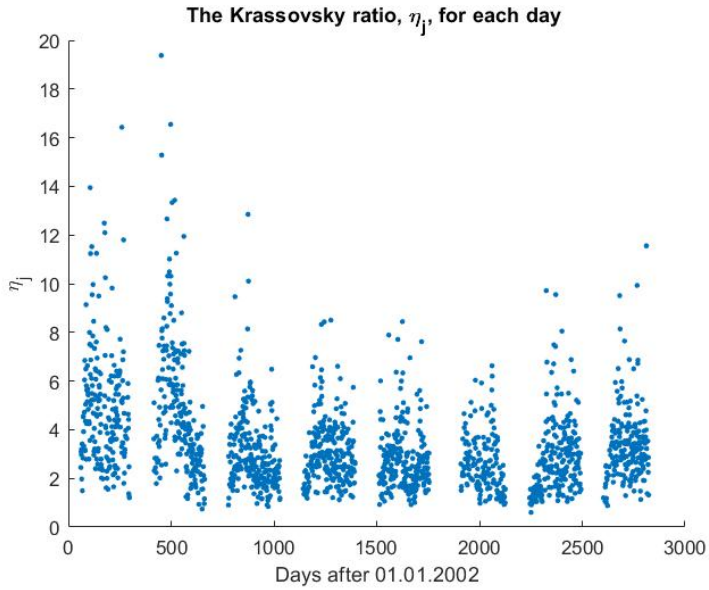

(b) The Krassovsky ratio for each DoM.

Figure 3.4: Scatter plot showing the Krassovsky ratio.

3.4 Background wind profiles

As mentioned in Chapter 2.4 gravity waves with horizontal phase speed that equals the background wind speed will break and deposit its energy and momentum. Therefore it is of interest to compare the variance in temperature to the background wind profiles. Hibbins et al. (2005) have studied the background zonal wind profiles up to $100\,\mathrm{km}$ and created a model with monthly averages at Rothera. Each month is represented by a sixth order polynomial fit of the form

$$U(z) = \sum_{n=0}^{6} A_n z^n, \tag{3.12}$$

where A_n are the coefficients of the polynomial, and z is the height above ground in km. The zonal wind profile for November is shown in Figure 3.5.

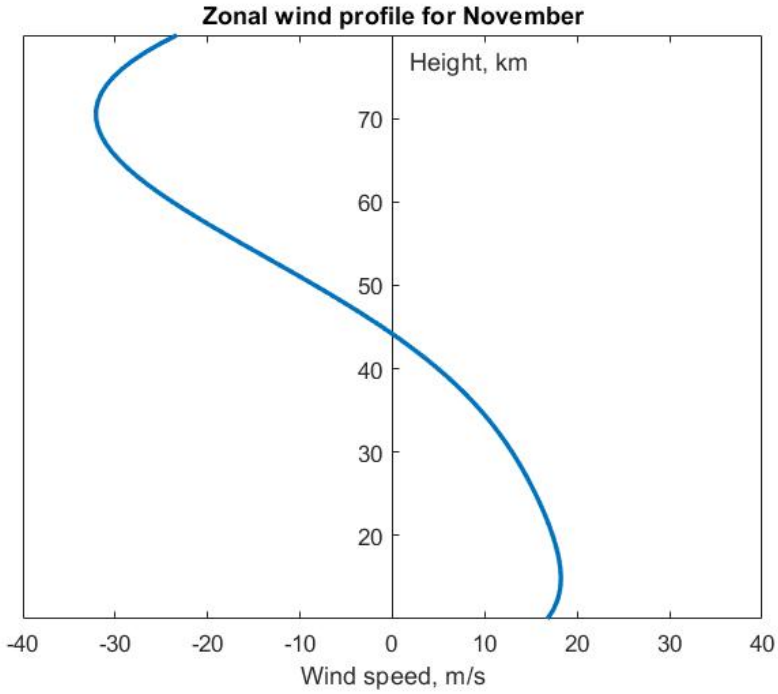

Figure 3.5: Zonal wind profile for November.

By assuming that all phase speeds, c, are equally probable, the range in wind speeds, $|U_{\text{max}} - U_{\text{min}}|$, was calculated and used as a measure of gravity wave blocking. Here $U_{\text{max}} = \max(0, U(z))$ and $U_{\text{min}} = \min(0, U(z))$. The assumption that all phase speeds are equally probable is a bit different from what is used by numerical weather and climate models. Most models use a spectrum, or a certain number of waves at each phase speed.

This can vary for mountains, frontal systems, or isolated thunderstorms. Here the source of the waves is unknown, and as such a uniform spectrum is used. While this may affect the absolute values, the trend with the underlying wind field should be the same. The range in zonal wind speeds for each month and monthly average of the climatological daily variance (henceforth referred to as climatological monthly variance) in temperature is shown in Figure 3.6a for all months of measurements, and in Figure 3.6b for the first four months of measurements.

For completeness sake the coefficients of correlation was calculated for all ten months of measurements, as well as the first part of the year. The coefficients of correlation is shown in Table 3.1. From the table one can see that using all ten months of measurements one would have to reject the hypothesis that the range in zonal wind speeds are correlated to the climatological monthly variance in temperature. This is however very much not the case if one removes the last part of the year.

# of months	R	RU	RL	P-value
4	-0.9773	-0.2663	-0.9995	0.0227
10	0.3144	0.8095	-0.4420	0.4100

Table 3.1: Coefficients of correlation for the range in zonal wind speeds and climatological monthly variance in temperature. The P-value is given, as well as R with corresponding upper and lower bounds for a 95% confidence interval.

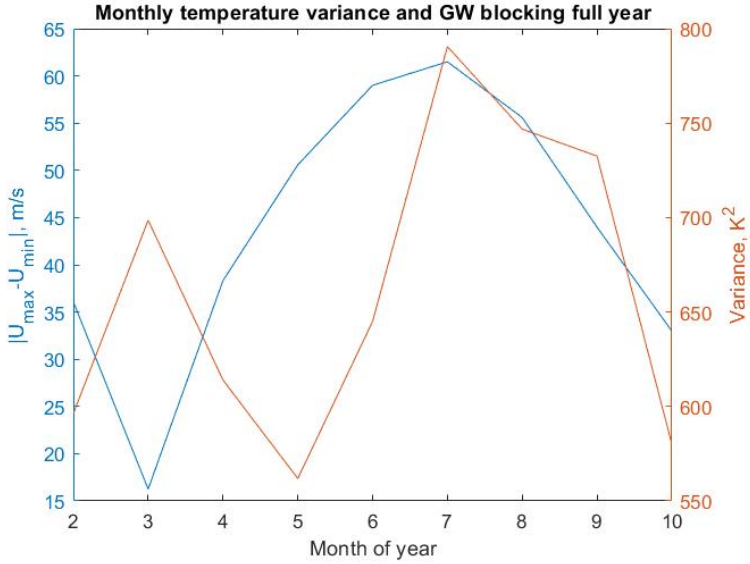

(a) GW blocking and climatological monthly variance in temperature.

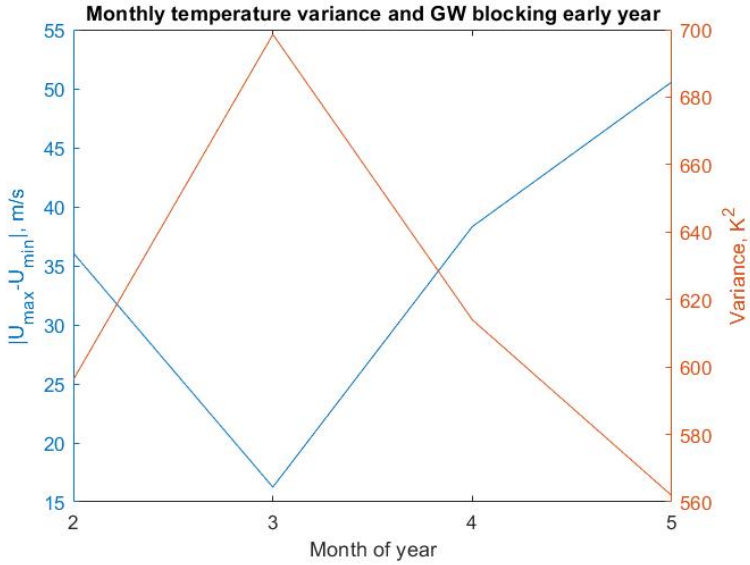

(b) GW blocking and climatological monthly variance in temperature for the first part of the year.

Figure 3.6: A dual line plot showing the range in zonal wind speed as a measure for gravity wave blocking in blue, and climatological monthly variance in temperature in red.

Chapter 4

Discussion

In this chapter the results from Chapter 3 will be discussed, and compared with results from other studies on gravity waves. Some of the assumptions made in the thesis will be questioned, and wherever it seems relevant some suggestions for future work will be proposed. In general this chapter is intended to provide some answers to the question of whether or not OH airglow measurements can be used to monitor the gravity wave activity of the mesosphere.

The first thing that need to be established is whether or not it is reasonable to assume that the results show gravity wave activity. From Figure 3.4a one sees that the bulk of the values of the Krassovsky ratio is between 2 and 6, with an average value of about 3.5. These numbers are commensurate to the ones calculated numerically by Swenson and Gardner (1998), as well as the measured values done by others as shown in the same article. This is a good indicator that the results indeed do show gravity wave activity. Figure 3.4b show the same ratio for all days of measurement. Here one notices some dates with values of over 15, as well as some days with values as low as 1. The bulk of the measurements are still in the desired range. These discrepancies can be attributed to the fact that some days have corrupted measurements due to technical difficulties, especially in the first years of measurement. This can cause gaps of up to a few hours in the measurements in the middle of the night. These large gaps can skew the calculated value of the mean if they happen at the start or end of the night, and can also cause a higher calculated deviation from the mean if it happens somewhere in the middle of the night. Another point of note here is that the calculated Krassovsky ratio is sensitive to the weather. The reason for this is that cloudy weather will block the measured intensity significantly, while the temperature remains about the same. This means that nights with unusually cloudy weather (yet not too cloudy for valid measurements) can affect the relative variance in intensity, which can potentially skew the results. Seeing as these effects are not prominent when looking at the climatology and the fact that they are easily explained, one still has a good indication that the results show gravity wave activity.

To fully determine whether we are indeed measuring gravity wave activity, the next thing to do is to look at how the results correlated with the averaged monthly range in zonal wind speed. Hibbins et al. (2005) used data from an MF radar, radiosonde balloon launches and falling sphere measurements to modify the empirical Horizontal Wind Model (HWM-93 model) to generate a new wind climatology showing the seasonal variation in the zonal wind field above Rothera station. The sixth order polynomial fit they generated was the one used to create Figure 3.5, and is the data used in Chapter 3.4 to get the monthly average values for zonal wind speed. Figure 4.1 show the entire climatology as presented in the article.

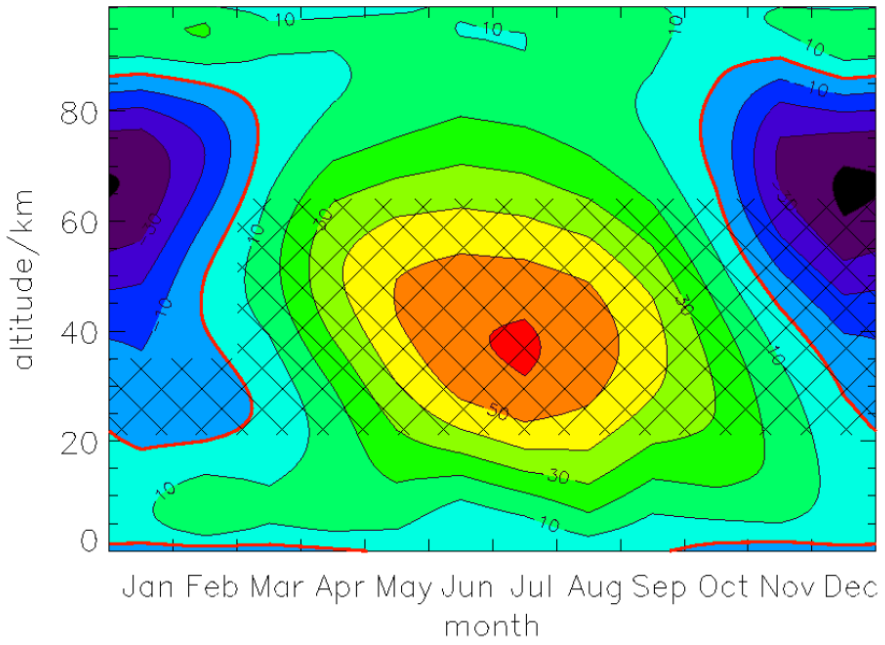

Figure 4.1: Mean zonal wind above Rothera from $0\,\mathrm{km}$ to $100\,\mathrm{km}$. Generated from 6th order polynomial fits to the monthly mean data and, within the hatched area, monthly mean HWM-93 model winds. The thick red line represents the $0\,\mathrm{m/s}$ contour, other contours are drawn at $10\,\mathrm{m/s}$ intervals (blue: westwards) (Hibbins et al., 2005).

From Figure 3.6a and Table 3.1 it is quite clear that comparing climatological daily variance in temperature with the range in mean zonal wind speeds is not the whole story. In Chapter 3.4 the claim was that if the gravity wave source function is of constant spectral power, then the intervening wind should control the number of waves reaching the mesosphere. When this was done with all months of measurements it gave a P-value of 0.41, which is way greater than the standard $\alpha = 0.05$ treshold for rejecting a null hypothesis. When looking at the months up until May however, one obtained a P-value of 0.02. For the first part of the year one also obtains a R-value of -0.9773 with both lower and upper bounds showing a negative correlation. According to the results, the original claim

holds for certain months. This would point towards there occasionally being changes in the gravity wave source function. This is in agreement with the results found by Hibbins et al. (2007). They notice that, although one would expect the gravity wave activity to peak when the underlying wind fields are at the minimum around the equinox, this is not the whole story. There seem to be increased activity in mid to late winter when the stratospheric winds should be greatest. They go on to conclude as follows: "This implies that either the tropospheric source of the gravity wave activity observed in the MLT above Rothera varies considerably throughout the year, or that a significant proportion of the gravity wave activity is generated from a region above the peak of the wintertime stratospheric jet" (Hibbins et al., 2007). This is in agreement with the results found in this thesis, and would further support why the claim posed here only holds for certain months.

Another possible explanation for the poor results when comparing to the last part of the year can be found from Venkateswara Rao et al. (2015) which have studied the background wind at Rothera using a MF Radar. They find that the wind speed in the late winter to spring has a larger year-to-year variance than fall and early winter. Venkateswara Rao et al. (2015) and references therein point to the increased loss in polar ozone as the main reason for this variability. Their studies show that "increased ozone loss causes temperatures in the polar stratosphere to remain colder as the heating by solar absorption is reduced. This leads to a prolongation of the large wintertime pole-to-equator temperature gradients, which, through thermal wind balance, maintain the strong wintertime eastward winds in the lower stratosphere longer into the early summer". A larger year-to-year variance in wind speed means that this part of the year is less reliable when comparing with the variance in temperature, and the second part of the year is therefore less likely to yield the anticorrelation that one would expect.

Due to the fact that there are some promising results, future work should try to compare tropospheric wind speed with mesospheric gravity wave power. Comparing the months where the hypothesis holds, to those where it does not would also be of interest. For a more complete investigation one should also compare with the meridional wind speeds. For the comparisons done in this thesis this has been omitted due to the fact that they are - in general - an order of magnitude weaker than the zonal wind speeds.

There are still a few more things to note. Looking at Figure 4.1 one does in fact see different ways in which the wind direction changes between the autumnal and the spring equinox. The change around autumnal equinox is characterized by a stratospheric and mesospheric wind that changes from westward to eastward at all heights within about a month, with no discernible high velocity wind at any altitude. The change around spring equinox on the other hand is quite different. At spring equinox, in late September, one still sees no westward winds at any altitudes, but rather eastward winds of up to $30\,\mathrm{m/s}$ to $40\,\mathrm{m/s}$. The change into westward winds start at high altitudes in October, although one still has altitudes of about $30\,\mathrm{m/s}$ eastward. These fundamental differences, along with the increased variability could help to explain why the second part of the year correlates a lot less with the results in this thesis.

The next thing to do is to compare the results with other measurements of gravity wave

activity. Hibbins et al. (2007) have used a MF radar to develop a climatology of gravity wave activity over Rothera using variance in zonal wind speed. Four of the years used in the development of the climatology overlaps with the data for this thesis. This climatology is shown in Figure 4.2. For ease of comparison the area that represents the OH airglow layer has been highlighted, and can be seen inside the black rectangle.

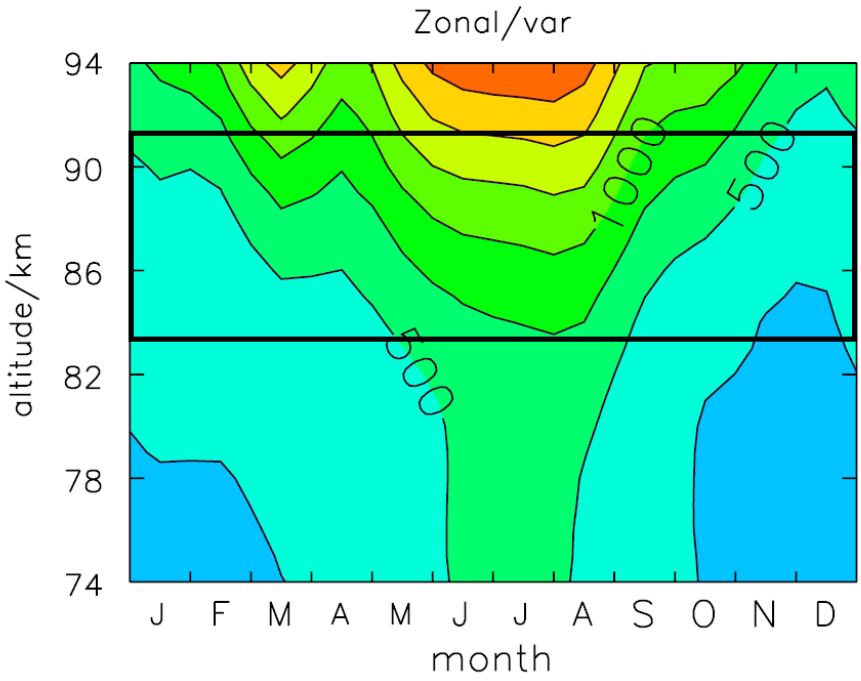

Figure 4.2: Monthly mean variance of the raw winds after subtracting tidal components and system noise. Contours are plotted at $250\,\mathrm{m}^2/\mathrm{s}^2$ intervals (Hibbins et al., 2007). Superposed is a rectangle to highlight the OH airglow layer.

For comparison, the average values from Figure 4.2 needed to be estimated and then converted into a line plot. Values for every half month was estimated, and then an average for the month was calculated. The estimated wind speed variance was then plotted together with the climatological monthly variance in temperature variance, and is shown in Figure 4.3.

The estimated variance in wind speed seemed to be commensurate with the average temperature variance, and as such the correlation coefficients was calculated. This gave a R-value of 0.678, with upper and lower limit of 0.025 and 0.925, and a P-value of 0.045. In other words about 46% of the values lie within one standard deviation of each other, which is about what one would expect for a Gaussian distribution of differences. Another thing to note is that the correlation is always positive at the 95% confidence level. This is a very good indicator that at least some of the variance measured are due to gravity wave activity. Further studies should be done with better filtering, and compared to MF

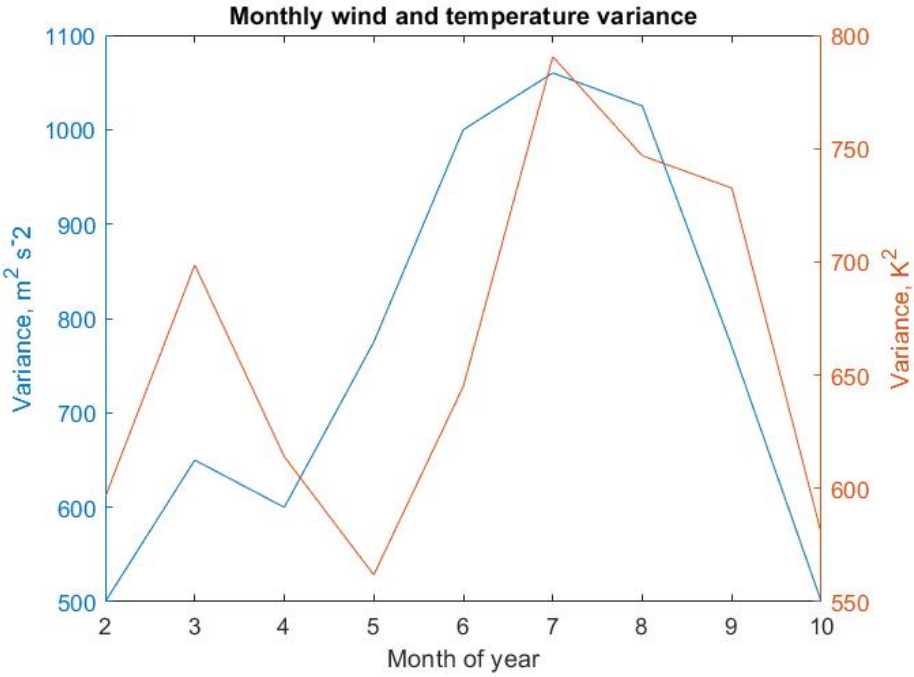

Figure 4.3: Monthly mean variance in wind speed (blue,left y-axis) plotted together with monthly mean variance in temperature (red, right y-axis).

radar wind speed measurements. It would also be of interest to study the correlation with a higher temporal resolution. Looking at Figure 4.3 one notices that there is only between the month of April and May that the two results do not show the same general trend. This is something that could be an artifact of the low temporal resolution.

The results in this thesis show that there are good reasons to believe that one indeed can use OH airglow measurements to monitor gravity wave activity. The question one needs to answer next is whether this is worth doing. That is, if there are any pros or cons in using this method. Interferometers like the one used here are really cheap, especially when compared to e.g. satellites. Making the measurements require very little human resources, seeing as the apparatus pretty much runs itself after setup. These instruments are abundant and therefore easily accessible for anyone who would want to set it up and start gathering data. There is really only one mayor downside here, and that is the fact that it is weather dependent. It can't obtain results in really cloudy weather. This is however also the case for pretty much all ground based measuring devices, and compared to e.g. a Lidar it is better suited for dealing with low levels of clouds.

Chapter 5

Conclusion

The initial goal of this thesis was to ascertain whether or not measuring the variance in temperature using an interferometer can be used as a proxy for gravity wave activity. To do this we first had to see if our measurements did indeed show gravity wave activity, and then to compare it with measurements obtained by others. The general agreement of the Krassovsky ratio derived here with other measurements show that the wave parameters derived here are generally commensurate with other airglow observations.

Comparisons with the range in zonal wind speeds of the underlying atmosphere is in very good agreement with the results for the first part of the year. This is however not the case if one includes late winter and spring, where the year-to-year variability in wind speed is much higher. The anticorrelation observed when comparing with the first part of the year yield a R-value of -0.98 with a P-value of 0.023, which points quite clearly towards the variance in temperature being a good measure for gravity wave activity.

Comparisons with previous estimates of gravity wave activity using variance in wind speed show promising results. The estimated variance in wind speed seemed to be commensurate with the average temperature variance. The correlation coefficients was calculated. This gave a R-value of 0.678, with upper and lower limit of 0.025 and 0.925, and a P-value of 0.045. The correlation was always positive at the 95$\%$ confidence level.

It seems that ground based studies of the OH airglow layer can be used to study gravity wave activity. Further studies are however needed to be able to say with any certainty if it can be used as a measure of gravity wave activity for the last part of the year.

Bibliography

Baker, D.J., Romick, G.J., 1976. The rayleigh: interpretation of the unit in terms of column emission rate or apparent radiance expressed in si units. Applied optics 15, 1966–1968.

Beldon, C., Mitchell, N., 2009. Gravity waves in the mesopause region observed by meteor radar, 2: Climatologies of gravity waves in the antarctic and arctic. Journal of Atmospheric and Solar-Terrestrial Physics 71, 875–884.

British Antarctic Survey UK Polar Data Centre, N., 2016, accessed 04.04.2020. Data coverage - all data selected. URL: `http://psddb.nerc-bas.ac.uk/data/access/coverage.php?menu=4&source=1&class=46&script=1`.

Espy, P., Hibbins, R., Jones, G., Riggin, D., Fritts, D., 2003. Rapid, large-scale temperature changes in the polar mesosphere and their relationship to meridional flows. Geophysical research letters 30.

Espy, P., Pendleton Jr, W., Sivjee, G., Fetrow, M., 1987. Vibrational development of the n2+ meinel band system in the aurora. Journal of Geophysical Research: Space Physics 92, 11257–11261.

Espy, P.J., Stegman, J., 2002. Trends and variability of mesospheric temperature at high-latitudes. Physics and Chemistry of the Earth, Parts A/B/C 27, 543–553.

Espy, P.J., Stegman, J., Forkman, P., Murtagh, D., 2007. Seasonal variation in the correlation of airglow temperature and emission rate. Geophysical research letters 34.

Franzen, C., Espy, P.J., Hibbins, R.E., 2020. Modelled effects of temperature gradients and waves on the hydroxyl rotational distribution in ground-based airglow measurements. Atmospheric Chemistry and Physics 20, 333–343.

Franzen, C., Hibbins, R., Espy, P.J., Djupvik, A.A., 2017. Optimizing hydroxyl airglow retrievals from long-slit astronomical spectroscopic observations .

Hemmer, P.C., 2005. Kvantemekanikk. 5 ed., Trondheim: Tapir Akademiske Forlag.

Herzberg, G., 1951. Molecular spectra and molecular structure. i. spectra of diatomic molecules .

Hibbins, R.E., Espy, P.J., Jarvis, M.J., Riggin, D.M., Fritts, D.C., 2007. A climatology of tides and gravity wave variance in the mlt above rothera, antarctica obtained by mf radar. Journal of Atmospheric and Solar-Terrestrial Physics 69, 578–588.

Hibbins, R.E., Shanklin, J.D., Espy, P.J., Jarvis, M.J., Riggin, D.M., Fritts, D.C., Lübken, F.J., 2005. Seasonal variations in the horizontal wind structure from 0-100 km above rothera station, antarctica (67 s, 68 w) .

Hickey, M.P., Yu, Y., 2005. A full-wave investigation of the use of a "cancellation factor" in gravity wave–OH airglow interaction studies. Journal of Geophysical Research: Space Physics 110.

Hines, C.O., Tarasick, D.W., 1987. On the detection and utilization of gravity waves in airglow studies. Planetary and space science 35, 851–866.

Hocking, W.K., 2001, accessed 24.02.2020a. Buoyancy (gravity) waves in the atmosphere. URL: `http://www.physics.uwo.ca/~whocking/p103/grav_wav.html`.

Hocking, W.K., 2001, accessed 24.02.2020b. Corrugated sheet. URL: `http://www.physics.uwo.ca/~whocking/p103/grav_cor.gif`.

Hunten, D.M., Roach, F.E., Chamberlain, J.W., 1956. A photometric unit for the airglow and aurora. Journal of Atmospheric and terrestrial Physics 8, 345–346.

Liu, A.Z., Swenson, G.R., 2003. A modeling study of o2 and oh airglow perturbations induced by atmospheric gravity waves. Journal of Geophysical Research: Atmospheres 108.

Lowe, R.P., LeBlanc, L.M., Gilbert, K.L., 1996. Windii/uars observation of twilight behaviour of the hydroxyl airglow, at mid-latitude equinox. Journal of Atmospheric and Terrestrial Physics 58, 1863–1869.

Lund, H., 2010. Variation of the hydroxyl near infrared airglow at rothera, antarctica (68s, 68w).

McQuarrie, D.A., Simon, J.D., 1997. Physical chemistry: a molecular approach. volume 1. University science books Sausalito, CA.

Mies, F.H., 1974. Calculated vibrational transition probabilities of oh (x2π). Journal of Molecular Spectroscopy 53, 150–188.

Mitchell, N.J., Beldon, C.L., 2009. Gravity waves in the mesopause region observed by meteor radar: 1. a simple measurement technique. Journal of Atmospheric and Solar-Terrestrial Physics 71, 886–874.

OpenStax, 2018, accessed 25.03.2020a. Electronic transitions. URL: https://chem.libretexts.org/Bookshelves/Physical_and_Theoretical_Chemistry_Textbook_Maps/Map%3A_Physical_Chemistry_(McQuarrie_and_Simon)/13%3A_Molecular_Spectroscopy/13.06%3A_Electronic_Spectra_Contain_Electronic%2C_Vibrational%2C_and_Rotational_Information.

OpenStax, 2018, accessed 25.03.2020b. Electronic transitions. URL: https://chem.libretexts.org/Courses/University_of_California_Davis/UCD_Chem_110B%3A_Physical_Chemistry_II/Text/13%3A_Molecular_Spectroscopy/13-02._Rotational_Transitions_Accompany_Vibrational_Transitions.

Pautet, P.D., Taylor, M.J., Pendleton, W.R., Zhao, Y., Yuan, T., Esplin, R., McLain, D., 2014. Advanced mesospheric temperature mapper for high-latitude airglow studies. Applied optics 53, 5934–5943.

SFSU, 2018, accessed 24.02.2020. Vertical temperature structure. URL: http://tornado.sfsu.edu/geosciences/classes/m100/Atmosphere/VerticalStructure.jpg.

Swenson, G.R., Gardner, C.S., 1998. Analytical models for the responses of the mesospheric OH and Na layers to atmospheric gravity waves. Journal of Geophysical Research: Atmospheres 103, 6271–6294.

Venkateswara Rao, N., Espy, P.J., Hibbins, R.E., Fritts, D.C., Kavanagh, A.J., 2015. Observational evidence of the influence of antarctic stratospheric ozone variability on middle atmosphere dynamics. Geophysical Research Letters 42, 7853–7859.

de Wit, R.J., 2015. Quantifying the influence of the stratosphere on the mesosphere and lower thermosphere.

NTNU

Norwegian University of
Science and Technology